AIAA JOURNAL
Vol. 32, No. 3, March 1994

General Solution Procedure for Flows in Local Chemical Equilibrium

Carey F. Cox* and Pasquale Cinnella†
Mississippi State University, Mississippi State, Mississippi 39762

This study details the derivation and application of an approximate Riemann solver of the Roe type specifically designed for the numerical simulation of inviscid and viscous flow problems involving general and virtually arbitrary mixtures of thermally perfect gases in local chemical equilibrium. The solution procedure is by no means limited to airflows and will be applied to an oxygen/hydrogen mixture as well. A "black box" solver for the local equilibrium composition of a gas mixture of known density and internal energy is coupled with the flow solver, which is based on the newly derived flux-difference-split technique. A few test cases, including both external and internal flows, illustrate the capabilities and the overall efficiency of the flow solver.

Introduction

RECENT years have witnessed a renewed interest in hypersonic gasdynamics,[1] spurred by the desire to build high-speed commercial aircraft such as the National Aero-Space Plane (NASP) and to further space exploration. In this context, flow problems involving chemical activity of air and fuel/oxidizer mixtures have received widespread attention. Finite rate chemistry calculations have been successfully attempted by several investigators,[2] although the computational requirements associated with three-dimensional simulations over realistic geometries are very high when many chemical species and numerous chemical reactions have to be included in the flow model.[3] Compounding the problem is the fact that the actual *kinetics* of chemical reactions in gas mixtures of practical interest are not fully understood, and the uncertainties in reaction rate values can be very high.[4] On the other hand, flow simulations made by means of the local chemical equilibrium assumption have the potential of yielding results at a fraction of the computational cost associated with an equivalent finite rate calculation.

A flow solver based on local chemical equilibrium will have to include five equations in three space dimensions instead of $N + 4$ that are necessary for a finite rate solver, where N is the number of chemical species. Moreover, the equilibrium composition of a mixture of gases is well known from classical thermodynamics,[5] and the thermodynamic data for gaseous species are well established. Unfortunately, local chemical equilibrium is only a *limiting case* of the "real life" finite rate chemistry, with the limit taken for reaction rates going to infinity,[6] and the accuracy of its predictions should be investigated for each class of problems of interest. Nevertheless, the aforementioned numerical and physical difficulties associated with finite rate simulations render local chemical equilibrium a very attractive tool for the scientist and the engineer, in particular when the driving consideration is a relatively inexpensive inclusion of "real-gas" effects.

Flow simulations in local chemical equilibrium have been attempted by several investigators. Davy et al.[7] present viscous calculations for a Jovian atmospheric entry; Désidéri et al.[8] compare blunt-body calculations made with a five-species air model and both local chemical equilibrium and finite rate chemistry; Liou[9] applies a three-dimensional parabolized Navier-Stokes (PNS) code to internal flows of equilibrium air; and Wang and Chen[10] and Collins et al.[11] study hydrogen/air mixtures in engine nozzles.

In the present study, a methodology is presented that is applicable to virtually *any* mixture of thermally perfect gases in local chemical equilibrium. A "black box" solver,[6,12] capable of evaluating the equilibrium composition and temperature of a mixture of gases at constant density and internal energy, is coupled to a three-dimensional flow solver for the thin-layer Navier-Stokes equations. A newly developed approximate Riemann solver of the Roe type is presented and employed for the space discretization. The approach undertaken is compatible with both finite rate and perfect-gas models,[6] thus allowing for comparisons between the different thermochemical models. Only minor modifications to existing perfect-gas codes would be necessary to implement the local chemical equilibrium capabilities, and the approximate Riemann solver reduces nicely to the standard algorithm developed by Roe[13] in the limit of no chemical activity.

The composition and thermophysical properties of dissociating and ionizing air have been curvefitted for a wide range of state variables, and the curvefits have been extensively employed for simulations of flows in local chemical equilibrium.[5,9] Although a curvefit calculation is very competitive in terms of computational requirements, the present approach is more general, because it is not limited to a specific mixture, albeit as important as air.

In the following, the basic thermodynamic properties of mixtures of thermally perfect gases in local chemical equilibrium will be described. The governing equations for a real-gas flow will be presented, including a few considerations on the modeling of transport properties. The numerical formulation adopted will be briefly introduced and the approximate Riemann solver derived in some detail. A few numerical results for both inviscid and viscous test cases will illustrate the capabilities of the code and the efficiency of the proposed approach.

Real-Gas Mixtures

Thermodynamic Model

At high temperatures, imperfect-gas effects are due to chemical changes in the amount of mass of each species and to the activation of internal energy modes that behave nonlinearly with temperature. As long as the pressure is sufficiently low, away from the gas triple point, each species of the gas mixture will behave as a thermally perfect gas. Moreover, if the flowfield is assumed to be in local chemical equilibrium, then it follows from thermodynamic considerations that only

Presented as Paper 93-0892 at the AIAA 31st Aerospace Sciences Meeting, Reno NV, Jan. 11-14, 1993; received March 24, 1993; revision received July 20, 1993; accepted for publication July 22, 1993.

*Postdoctoral Fellow, Engineering Research Center for Computational Field Simulation, P.O. Box 6176. Member AIAA.

†Assistant Professor, Department of Aerospace Engineering, P.O. Box 6176. Member AIAA.

two state variables are necessary to describe its condition at a given time and for every point in space.

In the following, a gas mixture composed of N species is employed, and density ρ and temperature T are selected as the two fundamental state variables. The internal energy e can be expressed in terms of species contributions employing the usual mixing rule

$$e = \sum_{s=1}^{N} Y_s e_s = \sum_{s=1}^{N} Y_s \left[\int_{T_{\text{ref}}}^{T} c_{v_s}(\tau)\, \mathrm{d}\tau + h_{f_s} \right] \tag{1}$$

where the species mass fraction $Y_s = Y_s(\rho, T) = \rho_s/\rho$, and the species specific heat at constant volume $c_{v_s} = c_{v_s}(T)$ have been introduced. In the previous equation, h_{f_s} is the species heat of formation at the reference temperature T_{ref}.

The *equilibrium* specific heats can be obtained as functions of temperature and density derivatives of the mass fractions, as follows:

$$c_v = \left(\frac{\partial e}{\partial T}\right)_v = \tilde{c}_v + \sum_{s=1}^{N} e_s \frac{\partial Y_s}{\partial T}$$

$$c_p = \left(\frac{\partial h}{\partial T}\right)_p = c_v + \frac{\tilde{R} + T \sum_{s=1}^{N} R_s (\partial Y_s/\partial T)}{\tilde{R} + \rho \sum_{s=1}^{N} R_s (\partial Y_s/\partial \rho)} \left(\tilde{R} - \frac{\rho}{T} \sum_{s=1}^{N} e_s \frac{\partial Y_s}{\partial \rho} \right) \tag{2}$$

where the mixture enthalpy $h = e + \tilde{R}T$ has been introduced, and the gas constant $\tilde{R}$ and the frozen specific heats $\tilde{c}_v$ and $\tilde{c}_p$ can be obtained from the mixture rule, as follows:

$$\tilde{R} = \sum_{s=1}^{N} Y_s R_s, \qquad \tilde{c}_v = \sum_{s=1}^{N} Y_s c_{v_s}$$
$$\tilde{c}_p = \sum_{s=1}^{N} Y_s c_{p_s} = \tilde{c}_v + \tilde{R} \tag{3}$$

Unless otherwise noted, partial derivatives with respect to the temperature are taken at constant density and vice versa.

The *thermal* equation of state, which is a relationship between pressure and temperature, is given by Dalton's law:

$$p = \sum_{s=1}^{N} \rho_s R_s T = \rho \tilde{R} T \tag{4}$$

The state relationship of the pressure to the specific internal energy occurs implicitly through the temperature. For a given chemical composition and internal energy, the temperature must be evaluated from the *caloric* equation of state, Eq. (1).

Speed of Sound

The speed of sound for a mixture in local chemical equilibrium is determined to be[6]

$$a^2 = \left(\frac{\partial p}{\partial \rho}\right)_s = \Gamma \frac{p}{\rho} = \Gamma \tilde{R} T \tag{5}$$

where the isentropic index $\Gamma = \Gamma(\rho, T)$ is given by the following:

$$\Gamma = \bar{\gamma} + \frac{\rho}{\tilde{R}T} \sum_{s=1}^{N} \frac{\partial Y_s}{\partial \rho} [R_s T - (\bar{\gamma} - 1) e_s]$$
$$\bar{\gamma} = \frac{\partial h/\partial T}{\partial e/\partial T} = 1 + \frac{\tilde{R} + T \sum_{s=1}^{N} R_s (\partial Y_s/\partial T)}{c_v} \tag{6}$$

In the previous equation, $\bar{\gamma}$ is the ratio of the partial derivative of enthalpy with respect to temperature *at constant density* to the partial derivative of the internal energy with respect to temperature, where the latter is the specific heat at constant volume c_v. The use of the isentropic index preserves the simplicity of the formula for the sound speed, but the functional dependence of this index from density and temperature is relatively involved.

There are at least four different "gammas" that can be defined for a gas in chemical equilibrium: the isentropic index Γ, the ratio of specific heats γ, the ratio of frozen specific heats $\tilde{\gamma} = \tilde{c}_p/\tilde{c}_v$, and the ratio of enthalpy and internal energy derivatives $\bar{\gamma}$. For a frozen flow, all four of these quantities will reduce to the same value, but for general flow conditions their values will remain different.

Black Box Solver

In a gas mixture in local chemical equilibrium, the knowledge of two state variables is sufficient to determine the mixture composition and all of the other thermodynamic state variables. For flows in local chemical equilibrium, it follows from a careful consideration of the governing equations that the two state variables that can be assumed to be known are density and internal energy.[6,12] The present study employs a black box solver for the determination of the chemical equilibrium composition of an arbitrary mixture of thermally perfect gases at constant density and internal energy,[6,12] which allows the user to choose between two different techniques. The first one utilizes a modified form of the laws of mass action in addition to elemental mass constraints, plus an energy equation. The second approach exploits the concept of degree of advancement of a chemical reaction to reduce the number of equations to be solved at each iteration. Both techniques have been proven to be robust and efficient, although the former method seems to be slightly more robust and the latter slightly more efficient.[12]

After the equilibrium composition is determined, the different thermodynamic state variables can be evaluated. Some of them require the knowledge of the partial derivatives of the mass fractions with respect to temperature and density, e.g., Eq. (6). The black box is capable of providing these values at virtually no extra cost.[6]

The numerical algorithm chosen for both techniques is a Newton-Raphson linearization, followed by a direct inversion of the resulting linear systems, performed by means of a lower-upper (LU) decomposition of the Jacobian matrix. The algorithms vectorize over the number of computational cells, and they are easily implemented in a massively parallel architecture. To reduce the global CPU time for equilibrium calculations, strategies for selective freezing of the LU decomposition have been studied and implemented.[6]

Governing Equations

Flow Equations

The governing differential equations for a gas in local chemical equilibrium, using generalized curvilinear coordinates, read

$$\frac{\partial}{\partial t}\left(\frac{\boldsymbol{Q}}{J}\right) + \frac{\partial(\tilde{\boldsymbol{F}} - \tilde{\boldsymbol{F}}_v)}{\partial \xi} + \frac{\partial(\tilde{\boldsymbol{G}} - \tilde{\boldsymbol{G}}_v)}{\partial \eta} + \frac{\partial(\tilde{\boldsymbol{H}} - \tilde{\boldsymbol{H}}_v)}{\partial \zeta} = 0 \tag{7}$$

where $\boldsymbol{Q}$ is the vector of conserved variables; $\tilde{\boldsymbol{F}}$, $\tilde{\boldsymbol{G}}$, and $\tilde{\boldsymbol{H}}$ are the inviscid flux vectors; $\tilde{\boldsymbol{F}}_v$, $\tilde{\boldsymbol{G}}_v$, and $\tilde{\boldsymbol{H}}_v$ are the viscous flux vectors; and J is the Jacobian of the transformation between Cartesian and generalized coordinates

$$J = \frac{\partial(\xi, \eta, \zeta)}{\partial(x, y, z)} \tag{8}$$

The vector $\boldsymbol{Q}$ reads

$$\boldsymbol{Q} = \begin{pmatrix} \rho \\ \rho u \\ \rho v \\ \rho w \\ \rho e_0 \end{pmatrix} \tag{9}$$

where u, v, and w are the Cartesian components of the velocity vector $\boldsymbol{u}$, whose magnitude will be denoted by q, and e_0 is the total internal energy, $e_0 = e + q^2/2$.

Denoting by $\tilde{S}$ the inviscid flux vector in the generic direction k, where $\tilde{S} = \tilde{F}$ when $k = \xi$, and similarly for the other space coordinates, one can write

$$\tilde{S} = \frac{|\Delta k|}{J} \begin{pmatrix} \rho\beta_k \\ \rho u\beta_k + \tilde{k}_x p \\ \rho v\beta_k + \tilde{k}_y p \\ \rho w\beta_k + \tilde{k}_z p \\ \rho\beta_k h_0 - \tilde{k}_t p \end{pmatrix} \tag{10}$$

where h_0 is the total enthalpy, $h_0 = h + q^2/2$; $\tilde{k}_x$, $\tilde{k}_y$, and $\tilde{k}_z$ are *normalized* metric terms, and β_k is the *relative* contravariant velocity component in the k direction

$$\beta_k = \theta_k + \tilde{k}_t, \qquad \theta_k = \tilde{k}_x u + \tilde{k}_y v + \tilde{k}_z w \tag{11}$$

which is the difference between the *absolute* contravariant velocity θ_k and the velocity associated with the time rate of change of the curvilinear coordinate $-\tilde{k}_t$.

In the present study, the viscous flux vectors are simplified by means of the thin-layer approximation,[14] which amounts to neglecting gradients of physical properties in all but one direction, the one normal to a solid wall. Denoting by $\tilde{S}_v$ the viscous flux vector in the direction k, normal to a solid wall, one can write, after some algebra,

$$\tilde{S}_v = \frac{|\Delta k|^2}{J} \begin{pmatrix} 0 \\ \mu\partial u/\partial k + \mu\tilde{k}_x u_k/3 \\ \mu\partial v/\partial k + \mu\tilde{k}_y u_k/3 \\ \mu\partial w/\partial k + \mu\tilde{k}_z u_k/3 \\ \kappa\partial T/\partial k + \mu\partial(q^2/2)/\partial k + \mu\theta_k u_k/3 \end{pmatrix} \tag{12}$$

where

$$u_k = \tilde{k}_x\frac{\partial u}{\partial k} + \tilde{k}_y\frac{\partial v}{\partial k} + \tilde{k}_z\frac{\partial w}{\partial k} \tag{13}$$

and the mixture viscosity coefficient μ and thermal conductivity coefficient κ have been introduced. More details on the derivation of appropriate values for μ and κ are given in the next subsection.

The previous equations do not include the effect of diffusion (transport of mass) due to inhomogeneity in composition between different points in the flowfield. Accounting for diffusion would require writing additional partial differential equations for the elemental species[7] and is beyond the scope of this study. Similarly, in agreement with most flowfield simulations involving gases, body forces (and gravity in particular) are neglected.

The mathematical closure to the system of partial differential equations presented is given by the thermal equation of state, Eq. (4), and the black box, which provides species mass fractions and temperature as functions of density and internal energy.

Transport Properties

Once the chemical composition of a point in the flowfield is known, the corresponding transport properties can be evaluated. The determination of *laminar* mixture viscosity μ and thermal conductivity κ usually proceeds in two steps: the species values are calculated first, and then an appropriate mixing rule is applied to determine the global values.[15] In the present study, two options have been implemented for the evaluation of species values: the first one is the commonly used Sutherland's law[14]; the second one is the curvefit tabulations by Gupta et al.,[15] which are valid for air chemistry models including up to 11 species. The mixture values are obtained by means of two different options as well: the "standard" Wilke's rule[3] and an improved mixture rule by Gupta et al.,[15] which involves tabulations of collision integrals for the same air models.

For turbulent flows, the viscosity and thermal conductivity are obtained by summation of laminar and turbulent contributions, where the Baldwin and Lomax model has been utilized for the turbulent quantities.[16]

Numerical Formulation

The governing equations presented in the previous section are discretized in space using upwind technology, in conjunction with finite volume ideas,[17] and advanced in time by means of a fully implicit scheme.[18] Specifically, the inviscid fluxes are discretized using an approximate Riemann solver of the Roe type, to be discussed in more detail in the next section. Standard central differences are utilized for the viscous fluxes. The implicit time integration is performed by means of the modified two-pass scheme.[18,19] The inviscid Jacobians that are needed for the left-hand side of the discretized equations are obtained from the analytical differentiation of a Steger-Warming-type solver.[20] In the derivation, the isentropic index Γ is assumed to be constant, in spite of the fact that it is a nonlinear function of temperature and density.[1,6,12] However, this assumption does not seem to affect the robustness and efficiency of the convergence process, as will be seen in the preliminary results obtained. The viscous Jacobians are obtained by a straightforward differentiation of the fluxes and are presented by Cox.[21]

Approximate Riemann Solver

Flux-difference-split algorithms are based on the approximate or exact solution of local Riemann problems arising from the consideration of discontinuous states at cell interfaces on an initial data line. The scheme developed for perfect gases by Roe[13] falls into this category and has produced excellent results for both inviscid and viscous flow simulations.

At a cell interface, for a given time, it is possible to define a left state, $(\cdot)_\ell$, and a right state, $(\cdot)_r$, which correspond to positive and negative extrapolations of cell-volume values, respectively. Then a *jump* operator may be defined as $[\![(\cdot)]\!] = (\cdot)_r - (\cdot)_\ell$. The key step in the construction of an approximate Riemann solver[22] involves determining appropriate averages of eigenvalues $\hat{\lambda}_i$, right eigenvectors $\hat{\boldsymbol{E}}_i$, and wave strengths $\hat{\alpha}_i$, such that

$$[\![\boldsymbol{Q}]\!] = \sum_{i=1}^{5} \hat{\alpha}_i \hat{\boldsymbol{E}}_i, \qquad [\![\tilde{S}]\!] = \sum_{i=1}^{5} \hat{\alpha}_i \hat{\lambda}_i \hat{\boldsymbol{E}}_i \tag{14}$$

for cell interface states that are not necessarily close to each other, so that $[\![\boldsymbol{Q}]\!]$ is arbitrary. The eigenvalues read

$$\hat{\lambda}_i = \frac{|\nabla k|}{J} \begin{cases} \hat{\beta}_k, & i = 1, 2, 3 \\ \hat{\beta}_k + \hat{a}, & i = 4 \\ \hat{\beta}_k - \hat{a}, & i = 5 \end{cases} \tag{15}$$

The eigenvectors are given as

$$\hat{\boldsymbol{E}}_1 = \begin{Bmatrix} \hat{\alpha}\tilde{k}_x \\ \hat{\alpha}\hat{u}\tilde{k}_x \\ \hat{\alpha}\hat{v}\tilde{k}_x + \hat{\rho}\tilde{k}_z \\ \hat{\alpha}\hat{w}\tilde{k}_x - \hat{\rho}\tilde{k}_y \\ \hat{\alpha}\tilde{k}_x[\hat{h}_0 - \hat{a}^2/(\hat{\gamma}-1)] + \hat{\rho}(\hat{v}\tilde{k}_z - \hat{w}\tilde{k}_y) \end{Bmatrix} \tag{16}$$

$$\hat{\boldsymbol{E}}_2 = \begin{Bmatrix} \hat{\alpha}\tilde{k}_y \\ \hat{\alpha}\hat{u}\tilde{k}_y - \hat{\rho}\tilde{k}_z \\ \hat{\alpha}\hat{v}\tilde{k}_y \\ \hat{\alpha}\hat{w}\tilde{k}_y + \hat{\rho}\tilde{k}_x \\ \hat{\alpha}\tilde{k}_y[\hat{h}_0 - \hat{a}^2/(\hat{\gamma}-1)] + \hat{\rho}(\hat{w}\tilde{k}_x - \hat{u}\tilde{k}_z) \end{Bmatrix} \tag{17}$$

$$\hat{E}_3 = \begin{Bmatrix} \hat{\alpha}\tilde{k}_z \\ \hat{\alpha}\hat{u}\tilde{k}_z + \hat{\rho}\tilde{k}_y \\ \hat{\alpha}\hat{v}\tilde{k}_z - \hat{\rho}\tilde{k}_x \\ \hat{\alpha}\hat{w}\tilde{k}_z \\ \hat{\alpha}\tilde{k}_z[\hat{h}_0 - \hat{a}^2/(\hat{\gamma}-1)] + \hat{\rho}(\hat{u}\tilde{k}_y - \hat{v}\tilde{k}_x) \end{Bmatrix} \tag{18}$$

$$\hat{E}_k = \hat{\alpha}\begin{pmatrix} 1 \\ \hat{u} \pm \hat{a}\tilde{k}_x \\ \hat{v} \pm \hat{a}\tilde{k}_y \\ \hat{w} \pm \hat{a}\tilde{k}_z \\ \hat{h}_0 \pm \hat{\theta}_k\hat{a} \end{pmatrix}, \qquad k = 4, 5 \tag{19}$$

and the wave strengths read

$$\begin{aligned} \hat{\alpha}_1 &= \frac{\tilde{k}_x}{\hat{\alpha}}\left([\![\rho]\!] - \frac{[\![p]\!]}{\hat{a}^2}\right) + \tilde{k}_z[\![v]\!] - \tilde{k}_y[\![w]\!] \\ \hat{\alpha}_2 &= \frac{\tilde{k}_y}{\hat{\alpha}}\left([\![\rho]\!] - \frac{[\![p]\!]}{\hat{a}^2}\right) - \tilde{k}_z[\![u]\!] + \tilde{k}_x[\![w]\!] \\ \hat{\alpha}_3 &= \frac{\tilde{k}_z}{\hat{\alpha}}\left([\![\rho]\!] - \frac{[\![p]\!]}{\hat{a}^2}\right) + \tilde{k}_y[\![u]\!] - \tilde{k}_x[\![v]\!] \\ \hat{\alpha}_k &= \frac{1}{\sqrt{2}}\left(\frac{[\![p]\!]}{\hat{\rho}\hat{a}} \pm [\![\hat{\theta}_k]\!]\right), \qquad k = 4, 5 \end{aligned} \tag{20}$$

where α is given by $\alpha = \rho/\sqrt{2}a$, and $\hat{\gamma} \equiv \tilde{\hat{\gamma}}$ is some average of the ratio of enthalpy and internal energy derivatives, defined in Eq. (6). The solution of the approximate Riemann problem involves determining algebraic averages $\hat{\rho}$, $\hat{u}$, $\hat{h}_0$, $\hat{\gamma}$, and $\hat{a}$, such that Eq. (14) are satisfied.

It is noteworthy that the aforementioned averages are *not unique*. As pointed out by Abgrall,[23] the algebraic problem posed in Eq. (14) has multiple solutions, and different values have been published in the literature for some of the Roe-type averages.[22-26] A careful examination of the different approaches shows that virtually the only discrepancy between them is in the evaluation of averages of the pressure derivatives with respect to density and internal energy. Abgrall,[23] unlike all of the other investigators already mentioned, considers a mixture of gaseous species in his derivation. The present approach is similar to the one he proposes but more clear and not limited to one chemical composition only. The other approaches are geared toward curvefit calculations and would not be easily applicable to problems involving arbitrary mixtures. More specifically, Vinokur[24] and Glaister[22] utilize relatively involved formulas for the pressure derivative averages, and Grossman and Walters[25] present a more approximate algorithm, valid for flows close to isentropic conditions.

In the present formulation, pressure derivatives are substituted by averages of $\bar{\gamma}$ and Γ. The final formulas will not become singular in smooth regions and will reduce nicely to the "usual" Roe averages for a perfect-gas model. Denoting the standard Roe average with the symbol $\mathcal{R}$, where

$$\mathcal{R}(\cdot) = \frac{[\sqrt{\rho_\ell}(\cdot)_\ell + \sqrt{\rho_r}(\cdot)_r]}{(\sqrt{\rho_\ell} + \sqrt{\rho_r})} \tag{21}$$

one determines the necessary averages as follows: $\hat{\rho}$ is given by the "usual" geometric average, $\hat{\rho} = \sqrt{\rho_\ell \rho_r}$; the velocity vector $\hat{u} = \mathcal{R}(u)$ (and similarly all of the Cartesian and contravariant components); and the total enthalpy $\hat{h}_0 = \mathcal{R}(h_0)$. The speed of sound $\hat{a}$ reads

$$\hat{a}^2 = \hat{\Gamma}\hat{R}\hat{T} + (\hat{\gamma}-1)\left(\hat{h}_0 - \frac{\hat{u}^2}{2} - \sum_{s=1}^{N}\hat{Y}_s\hat{e}_s - \hat{R}\hat{T}\right) \tag{22}$$

where

$$\begin{aligned} \hat{\Gamma} &= \hat{\gamma} + \frac{\hat{\rho}}{\hat{R}\hat{T}}\sum_{s=1}^{N}\overline{\frac{\partial Y_s}{\partial \rho}}[R_s\hat{T} - (\hat{\gamma}-1)\hat{e}_s] \\ \hat{\gamma} &= 1 + \frac{\hat{R} + \hat{T}\sum_{s=1}^{N}R_s(\overline{\partial Y_s/\partial T})}{\sum_{s=1}^{N}\hat{Y}_s\bar{c}_{v_s} + \sum_{s=1}^{N}\hat{e}_s(\overline{\partial Y_s/\partial T})} \end{aligned} \tag{23}$$

In the previous equations, mixture gas constant $\hat{R} = \mathcal{R}(\tilde{R})$, temperature $\hat{T} = \mathcal{R}(T)$, species internal energy $\hat{e}_s = \mathcal{R}(e_s)$, and mass fractions $\hat{Y}_s = \mathcal{R}(Y_s)$ are given by Roe-type averages. On the other hand, species specific heats at constant volume and mass fraction derivatives appeared in the previous expressions with a bar above them. These quantities are averaged by means of *integral* averages between the left and right states. Vinokur[24] discusses a procedure that would eliminate the discretization error involved in an approximate evaluation for these averages, but the final result is relatively involved. Instead, the simple trapezoidal rule has been used in the present study to approximate the integral average, which is tantamount to using the *arithmetic* average: $\bar{c}_{v_s} = [c_{v_s}(T_\ell) + c_{v_s}(T_r)]/2$, with similar results for the mass fraction derivatives.

The approximate Riemann solver is implemented by computing the cell fluxes at a generic face $(l + 1/2)$ as a summation over wave speeds

$$\tilde{S}_{l+\frac{1}{2}} = \tfrac{1}{2}(\tilde{S}_r + S_\ell) - \tfrac{1}{2}\sum_{i=1}^{5}\hat{\alpha}_i\,|\hat{\lambda}_i|\,\hat{E}_i \tag{24}$$

When the monotone upstream-centered schemes for conservation laws (MUSCL) approach is employed, right and left states are evaluated using high-order interpolation formulas, applied to primitive or characteristic variables. When the flux interpolation approach is utilized, the previous expression Eq. (24) corresponds to the first-order contribution, and high-order terms may be added[18,19] to render the scheme second- or third-order accurate. These additional terms will involve eigenvalues, right eigenvectors, and wave strengths, which have been given in Eqs. (15-20). The latter approach has been implemented in the present study.

Numerical Results

A few preliminary results in two space dimensions, both inviscid and viscous, are presented in the following. They include a Mach 10 external airflow over a blunt 9-deg half-angle cone, a simulation of the hydrogen/oxygen flow inside the Space Shuttle main engine (SSME) nozzle, and a Mach 10 airflow in a supersonic inlet. The airflow cases utilize a simple 5-species model,[6] which was found to yield essentially the same predictions as more refined 17-species models for the ranges of temperature and density of interest.[21] The hydrogen/oxygen flow involves six species, namely, O_2, H_2, OH, H_2O, O, and H. A second-order accurate space discretization with the Van Leer limiter,[18] in conjunction with the Riemann solver of the Roe type already discussed, was used for the first two calculations presented. A third-order accurate upwind biased scheme was employed for the third test case, and the minmod limiter was utilized.[18]

Blunt Cone, Inviscid

Figure 1 depicts the cone geometry and the 71 × 26 grid employed for the inviscid calculations. The nose radius is 2.5 in., or 6.35 cm. The freestream conditions are Mach number $M_\infty = 10$, zero angle of attack, pressure $p_\infty = 26.5 \times 10^3$ Pa, temperature $T_\infty = 223$ K, and density $\rho_\infty = 0.414$ kg/m^3. The results obtained with a perfect-gas thermochemical model are compared with those employing local chemical equilibrium.

Figure 2 shows temperature profiles along the stagnation streamline. Both temperature levels and shock location are strongly affected by the inclusion of real-gas effects. The

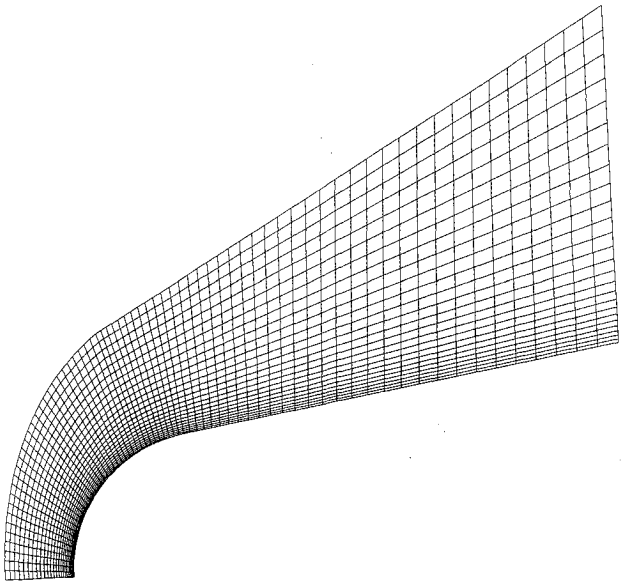

Fig. 1 Inviscid grid around a blunt cone with a 9-deg half-angle.

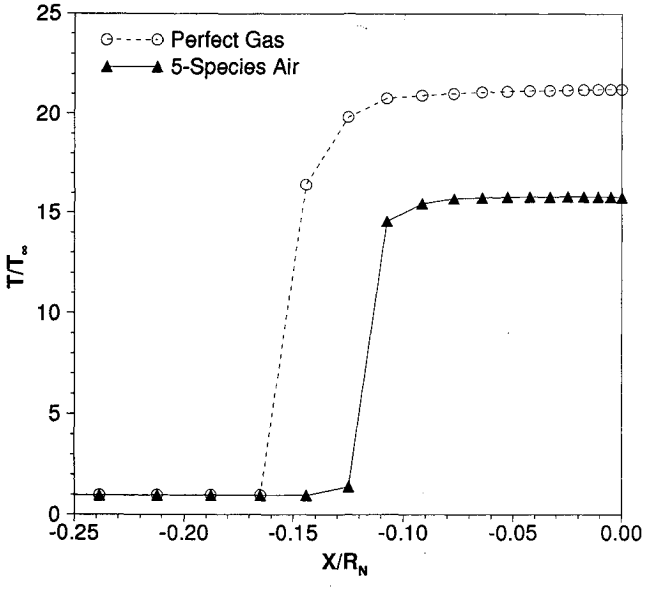

Fig. 2 Temperature vs distance along the stagnation streamline; blunt cone, inviscid.

perfect-gas results in this flow regime are unsatisfactory, as expected. The density profiles, not shown here, follow the same trend. Higher densities in the shock layer and shock locations closer to the body are characteristic of reactive flows.[1] A plot of the temperature on the body surface is shown in Fig. 3, and it depicts the cooling of the flow as it moves around the body. Although large temperature differences exist between the perfect-gas model and the reactive model in the nose region, the colder flow on the shoulder shows a good agreement between the two predictions. This is justified by examining the mixture composition on the body surface, reproduced in Fig. 4. The mixture is virtually all recombined in the frustrum region.

Unlike temperature and density, the pressure on the body is not strongly affected by the change in the thermochemical model. This is a well-known fact,[1] justified by the "mechanical" instead of "thermodynamic" nature of pressure.

Numerical Efficiency

The numerical efficiency of the local chemical equilibrium solver was investigated using the previous geometry as a test case. The CPU time and iteration number requirements of the solver were compared with the values obtained when running the perfect-gas model, and several CPU-saving techniques were implemented and tested on a Cray Y-MP.

The convergence strategy adopted for all calculations is the following: the first 100 cycles are run with a Courant-Friedrichs-Lewy (CFL) number of 0.5 and first-order space accuracy; the following 100 cycles are run with a CFL number of 1.0 and second-order upwind[19] accuracy; the next 100 cycles are run with a CFL number of 2.0; afterwards the CFL number is increased to 4.0 until a total of 1000 cycles is run, with a residual reduction of almost five orders of magnitude. The perfect-gas calculation was completed in roughly 3.5 CPU min.

Figure 5a shows the normalized residual reduction vs CPU time for the perfect-gas case and three different runs of the local chemical equilibrium code. The symbols on the chemical equilibrium curves correspond to the completion of 100 cycles. Case 1 is a baseline run, with the chemical equilibrium composition evaluated at every cycle, and it takes 53 CPU min to reach a comparable residual reduction. It may be noticed that

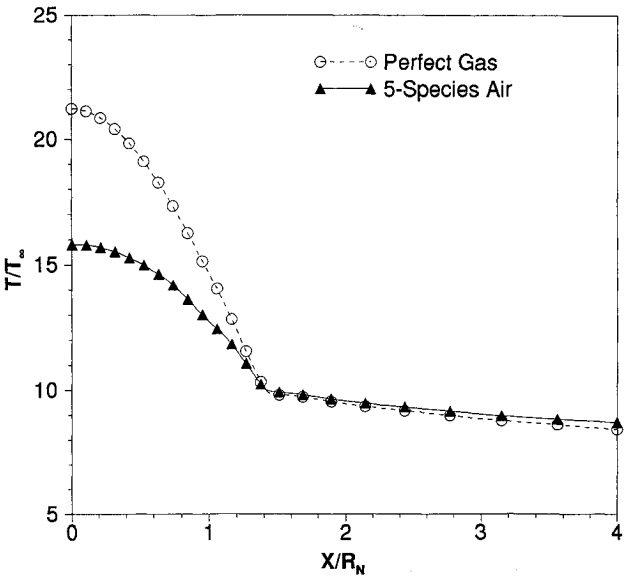

Fig. 3 Temperature vs distance along the body surface; blunt cone, inviscid.

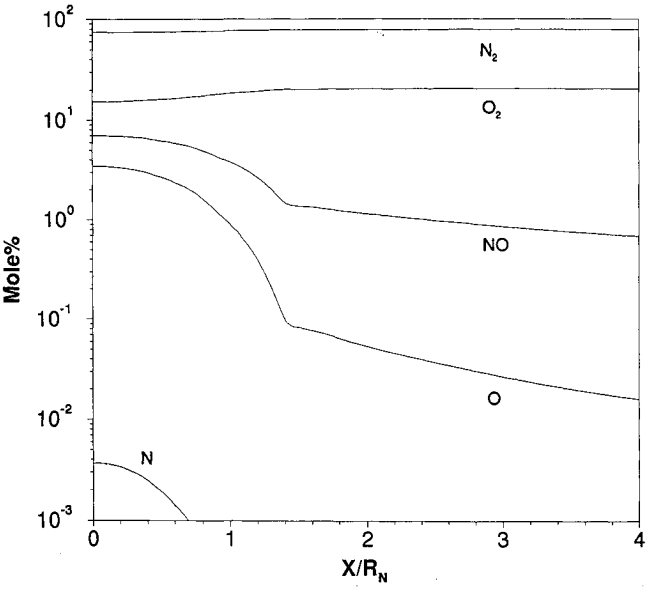

Fig. 4 Mole fractions vs distance along the body surface; blunt cone, inviscid.

a considerable amount of time is spent in the first few hundred cycles, when the solution goes through a numerical transient. However, even when convergence starts accelerating, the CPU requirements are very high for this case. This relative inefficiency was found to be caused by the procedure adopted to improve the vectorization of the black box. Specifically, the iterations that yielded chemical composition and temperature at every computational cell involved *all* of the cells of the flowfield, until *every one* of them converged. This strategy results in a large vector length for a vector processor (the entire number of computational cells) but requires carrying along an increasingly large number of converged cells, until convergence of the entire vector is achieved. At this point, a vector reduction capability was added to the code,[27] whereby the vector of computational cells that goes through an iteration is reorganized at the beginning of the iteration by eliminating the converged cells. Consequently, the vector has a length that varies from iteration to iteration, and some nonvectorizable logic is necessary to achieve vector reduction. However, the overhead associated with the process is significantly outweighed by the gained efficiency of the black box iterations. This is demonstrated by case 2 in Fig. 5a, which is similar to case 1 but employs the vector reduction procedure. The CPU time requirement is dramatically reduced.

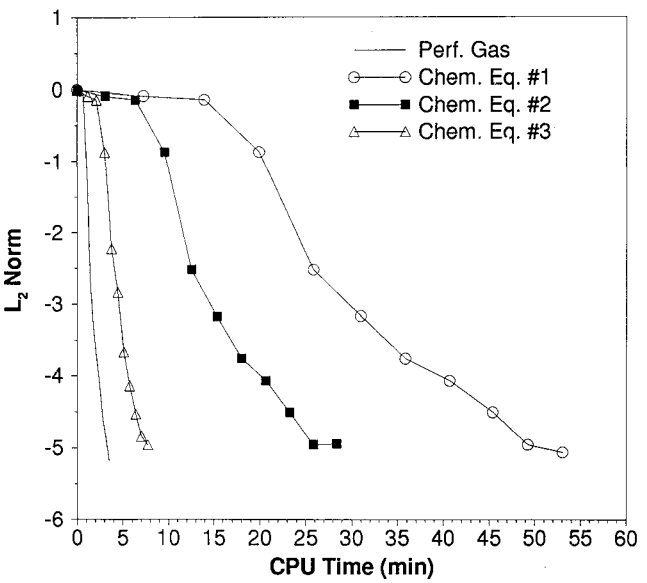

Fig. 5a Comparison of normalized residuals vs CPU time.

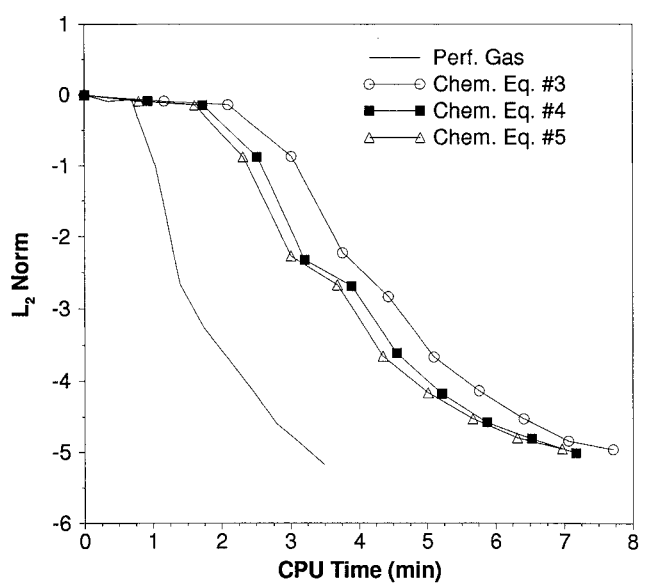

Fig. 5b Comparison of normalized residuals vs CPU time (concluded).

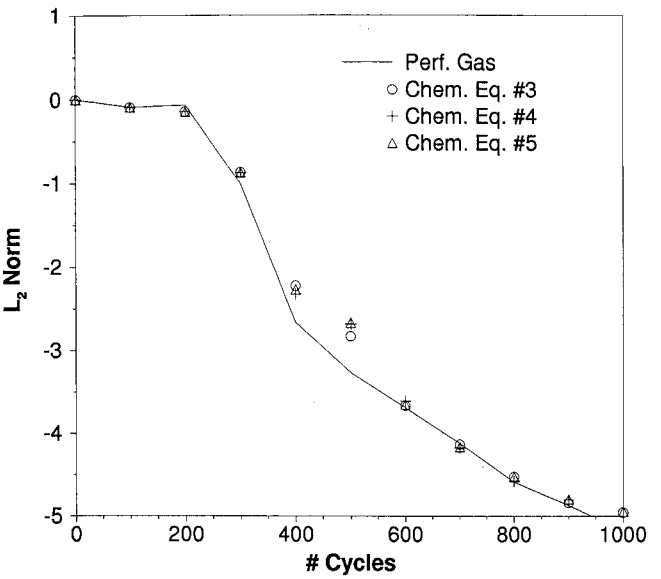

Fig. 6 Comparison of normalized residuals vs number of iterations.

Another significant reduction in CPU time requirements is achieved by starting some "freezing" procedures, whereby the chemical composition of each computational cell is not updated at every time step; instead it is frozen at the current value and updated after a specified number of cycles have been completed. In this procedure, the temperature is still updated every cycle by solving the caloric equation of state, Eq. (1), but the species mass fractions are not recalculated in the intermediate cycles. Case 3 shows a calculation performed by using the following procedure: the chemical composition is evaluated every 5 time steps for the first 100 cycles, every 10 time steps for the following 200 cycles, every 25 time steps for another 100 cycles, and then every 50 time steps until convergence. The final result is a run that takes approximately 7.7 min. It may be noticed from the picture that almost the entire additional CPU time that case 3 requires when compared with the perfect-gas run lies in the initial transient (first 200 cycles), when the flow is rapidly changing and the shock is moving from the body surface toward its final location.

A little improvement over case 3 is still possible, as shown in Fig. 5b, by experimenting with the freezing strategy. Case 4 implements the following procedure: chemical composition updated every 10 cycles for the first 100 time steps, every 20 cycles for the following 200 time steps, and every 50 cycles afterwards. The final result is somewhat improved, but the CPU requirements do not seem to be a very sensitive function of the specific strategy implemented. This conclusion seems to be confirmed by case 5, whereby the chemical composition is updated every 20 iterations for the first 200 cycles and every 50 iterations afterwards. It may be noticed from the plot that a very marginal improvement over case 4 in the first 200 cycles (the first two symbols) is then dissipated and translates into a negligible overall gain. The CPU time required for case 5 is approximately 7 min.

Figure 6 shows that all of the previous runs behave very similarly in terms of residual reduction vs number of cycles.

At this point, it may be useful to stress that finite rate calculations with five (or more) chemical species would require CPU times that are significantly more than a twofold increase over a perfect-gas calculation, as seen with the present technique.

SSME Nozzle, Inviscid

The geometry of the SSME nozzle and the 88 × 31 grid used for the inviscid computations were obtained from Wang and

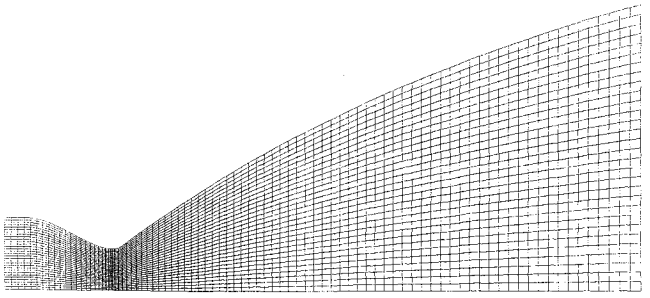

Fig. 7 Inviscid grid for the SSME nozzle.

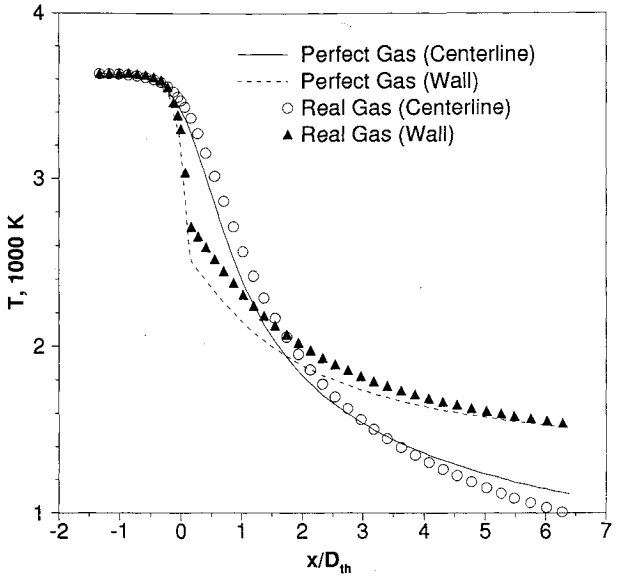

Fig. 8 Temperature vs axial distance; SSME nozzle, inviscid.

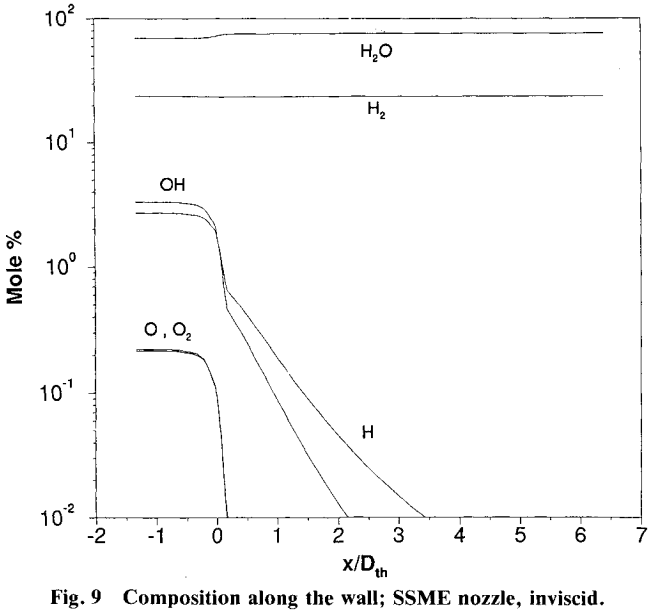

Fig. 9 Composition along the wall; SSME nozzle, inviscid.

Chen[10] and are shown in Fig. 7. Combustion chamber conditions correspond to 100% power at sea level and are hydrogen/oxygen ratio of 6.0, Mach number $M_c = 0.2$, temperature $T_c = 3639$ K, and pressure $p_c = 20.24 \times 10^6$ Pa. Simulations were made using both the perfect-gas model with $\gamma = 1.18$ and the six-species hydrogen/oxygen model already introduced.

The temperature profiles along the centerline and the wall of the nozzle are given in Fig. 8. The axial distances shown in this and the following figure are referenced to the throat location. Higher temperatures for the reacting solution occur, starting at a point just past the throat. As shown in Fig. 9, the flow in the diverging portion of the nozzle is dominated by recombination reactions, affecting hydrogen and oxygen, and successive combustion of the recombined species. Both sets of reactions are exothermic in nature.

Similar computations were made by Wang and Chen,[10] using a pressure-based flow solver and equilibrium chemistry. Comparisons of the real-gas solutions obtained in the present study with the results by Wang and Chen are made in Fig. 10, where the Mach number profiles are plotted. The figure shows excellent agreement between the two sets of results, with the exception of the throat region. The present method appears to do a better job of capturing the rapid expansion at the wall. It should be noted that Wang and Chen use artificial dissipation

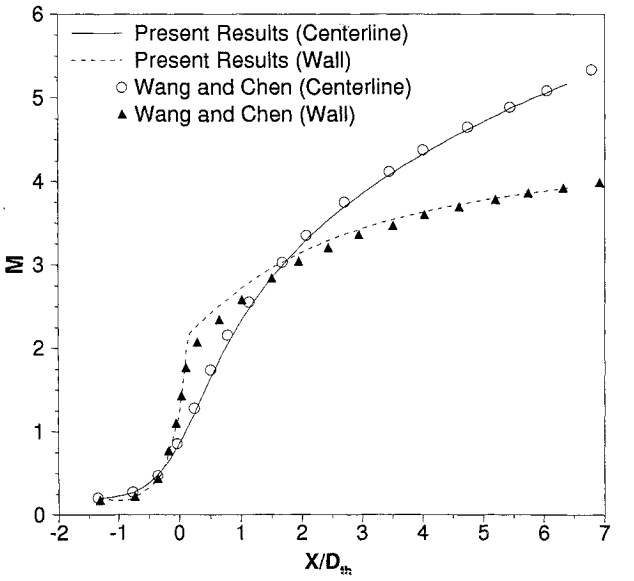

Fig. 10 Mach number vs axial distance; SSME nozzle, inviscid.

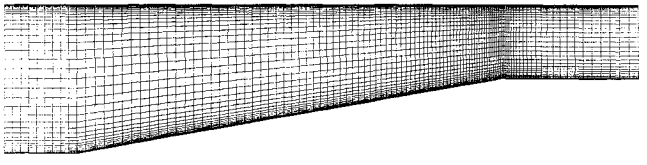

Fig. 11 Viscous grid for the supersonic inlet.

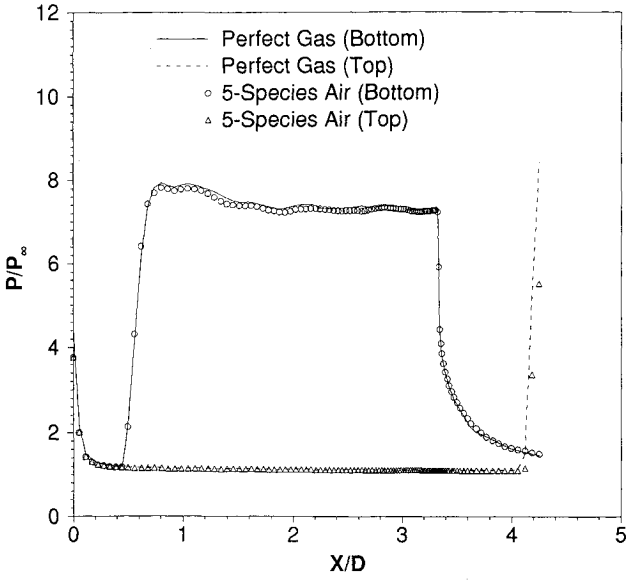

Fig. 12 Pressure vs axial distance; supersonic inlet, viscous.

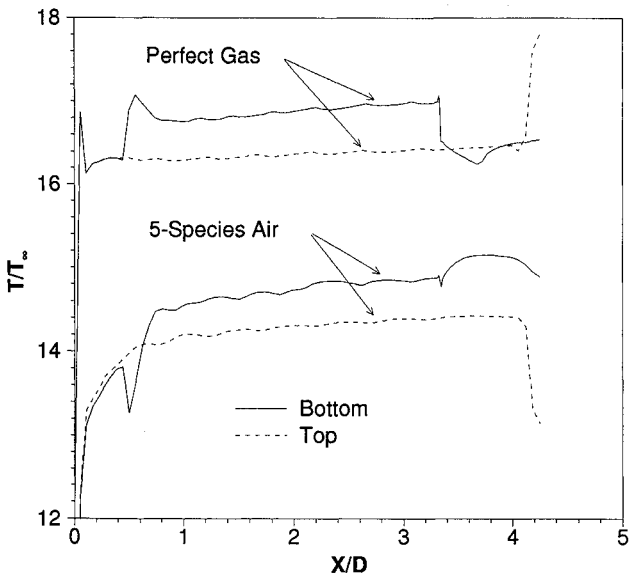

Fig. 13 Temperature vs axial distance; supersonic inlet, viscous.

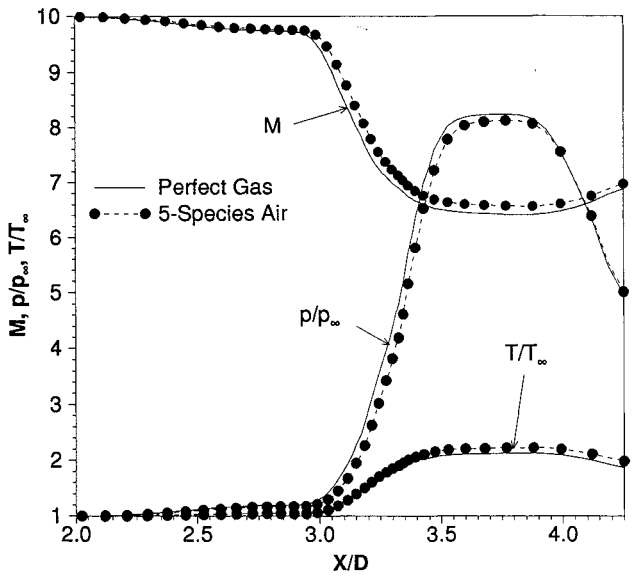

Fig. 14 Mach number, pressure, and temperature along the centerline; supersonic inlet, viscous.

in their scheme, which is probably the reason for the smearing of their results.

The specific impulse of the SSME nozzle was computed to be 460.0 s, which is also in excellent agreement with the value 460.4 s predicted by Wang and Chen.[10]

Supersonic Inlet, Viscous

The inlet considered is composed of a flat-surfaced cowl and a 10-deg ramp, with an inlet height $D = 2$ m and an exit height of $0.5D$. The overall length is $4.25D$, and the cowl length is $0.5D$. Conditions at the inlet are Mach number $M_\infty = 10$, pressure $p_\infty = 1015$ Pa, density $\rho_\infty = 1.172 \times 10^{-2}$ kg/m^3, temperature $T_\infty = 300$ K, and Reynolds number based on the inlet height $Re_D = 4.4 \times 10^6$. Figure 11 depicts the inlet geometry and the 111×61 grid used for the turbulent calculations, which were performed with both the perfect-gas model and the five-species air model. Grid packing at the wall resulted in y^+ values less than 1, which is considered adequate to define the viscous sublayer. Laminar viscosity and thermal conductivity coefficients were obtained by means of Wilke's rule and Sutherland's law.

The pressure profiles along the top and bottom walls of the inlet are represented in Fig. 12. They are not strongly affected by the consideration of local chemical equilibrium. The same holds true for the skin friction coefficient, not shown here. On the other hand, the temperature profiles, shown in Fig. 13, demonstrate that the perfect-gas model overpredicts temperature.

Examination of Mach number, temperature, and pressure profiles along the centerline, as depicted in Fig. 14, shows that there is very little difference between the solutions for the two thermochemical models other than the reduced shock angle for the reactive case. This results in the incident shock on the top wall for the reactive solution being located slightly downstream of the one for the perfect-gas solution. Overall, the real-gas effects are local to the boundary layer and have the greatest impact on the surface temperatures.

Concluding Remarks

An efficient flow solver has been developed for arbitrary mixtures of thermally perfect gases in local chemical equilibrium. An approximate Riemann solver of the Roe type has been proposed in the context of finite-volume technology for the accurate solution of high-velocity, high-temperature flow problems. The present approach compares favorably with existing calculations, and results in reactive flow predictions obtained at a fraction of the computational cost of finite rate chemistry investigations.

Future work is necessary to further validate the technique proposed in three space dimensions. Moreover, a multiblock extension of the present approach is being planned, which would allow the investigation of more complex geometries of practical interest.

Acknowledgments

This work was supported in part by the U.S. Air Force, Eglin Air Force Base, Florida, under Contract FO8635-89-C-0208, and in part by the National Science Foundation, which funds the Engineering Research Center for Computational Field Simulation. Both contributions are gratefully acknowledged.

References

[1]Anderson, J. D., Jr., *Hypersonic and High Temperature Gas Dynamics*, McGraw-Hill, New York, 1989.

[2]Grossman, B., and Cinnella, P., "Flux-Split Algorithms for Flows with Nonequilibrium Chemistry and Vibrational Relaxation," *Journal of Computational Physics*, Vol. 88, No. 1, 1990, pp. 131–168.

[3]Walters, R. W., Cinnella, P., Slack, D. C., and Halt, D., "Characteristic-Based Algorithms for Flows in Thermo-Chemical Nonequilibrium," *AIAA Journal*, Vol. 30, No. 5, 1992, pp. 1304–1313.

[4]Bauer, S. H., "Chemical Kinetics: A General Introduction," *Progress in Astronautics and Rocketry*, Vol. 7, 1962, pp. 143–180.

[5]Vincenti, W. G., and Kruger, C. H., Jr., *Introduction to Physical Gas Dynamics*, Krieger, Malabar, FL, 1986.

[6]Cinnella, P., and Cox, C. F., "An Efficient 'Black Box' Solver for the Equilibrium Composition of Real Gases," AIAA Paper 91-3322, Sept. 1991.

[7]Davy, W. C., Lombard, C. K., and Green, M. J., "Forebody and Base Region Real-Gas Flow in Severe Planetary Entry by a Factored Implicit Numerical Method—Part II: Equilibrium Reactive Gas," AIAA Paper 81-0282, Jan. 1981.

[8]Désidéri, J.-A., Glinsky, N., and Hettena, E., "Hypersonic Reactive Flow Computations," *Computers and Fluids*, Vol. 18, No. 2, 1990, pp. 151–182.

[9]Liou, M.-F., "Three Dimensional PNS Solutions of Hypersonic Internal Flows with Equilibrium Chemistry," AIAA Paper 89-0002, Jan. 1989.

[10]Wang, T., and Chen, Y., "A Unified Navier-Stokes Flowfield and Performance Analysis of Liquid Rocket Engines," AIAA Paper 90-2494, July 1990.

[11]Collins, F. G., Orr, J. L., and Myruski, B., "Modification of the PARC Navier-Stokes Code to Predict Rocket Engine Nozzle Performance," AIAA Paper 90-2491, July 1990.

[12]Cinnella, P., and Cox, C. F., "Robust Algorithms for the

Thermo-Chemical Properties of Real Gases," *Computational Fluid Dynamics Journal*, Vol. 1, No. 2, 1992, pp. 143–154.

[13]Roe, P. L., "Characteristic-Based Schemes for the Euler Equations," *Annual Review of Fluid Mechanics*, Vol. 18, 1986, pp. 337–365.

[14]Anderson, D. A., Tannehill, J. C., and Pletcher, R. H., *Computational Fluid Mechanics and Heat Transfer*, Hemisphere, New York, 1984.

[15]Gupta, R. N., Yos, J. M., Thompson, R. A., and Lee, K.-P., "A Review of Reaction Rates and Thermodynamic and Transport Properties for an 11-Species Air Model for Chemical and Thermal Nonequilibrium Calculations to 30000 K," NASA RP 1232, Aug. 1990.

[16]Baldwin, B. S., and Lomax, H., "Thin Layer Approximation and Algebraic Model for Separated Turbulent Flows," AIAA Paper 78-257, Jan. 1978.

[17]Walters, R. W., and Thomas, J. L., "Advances in Upwind Relaxation Methods," *State-of-the-Art Surveys on Computational Mechanics*, edited by A. K. Noor, American Society of Mechanical Engineers Publications, 1987, Chap. 4.

[18]Whitfield, D. L., Janus, J. M., and Simpson, L. B., "Implicit Finite Volume High Resolution Wave-Split Scheme for Solving the Unsteady Three-Dimensional Euler and Navier-Stokes Equations on Stationary or Dynamic Grids," Mississippi State Univ., EIRS Rept. MSSU-EIRS-ASE-88-2, Mississippi State, MS, Feb. 1988.

[19]Taylor, L. K., and Whitfield, D. L., "Unsteady Three-Dimensional Incompressible Euler and Navier-Stokes Solver for Stationary and Dynamic Grids," AIAA Paper 91-1650, July 1991.

[20]Vinokur, M., and Montagné, J.-L., "Generalized Flux-Vector Splitting for an Equilibrium Real Gas," NASA CR 177513, Dec. 1988.

[21]Cox, C. F., "An Efficient Solver for Flows in Local Chemical Equilibrium," Ph.D. Dissertation, Dept. of Mechanical Engineering, Mississippi State Univ., Mississippi State, MS, Dec. 1992.

[22]Glaister, P., "An Approximate Linearised Riemann Solver for the Three-Dimensional Euler Equations for Real Gases Using Operator Splitting," *Journal of Computational Physics*, Vol. 77, No. 2, 1988, pp. 361–383.

[23]Abgrall, R., "An Extension of Roe's Upwind Scheme to Algebraic Equilibrium Real Gas Models," *Computers and Fluids*, Vol. 19, No. 2, 1991, pp. 171–182.

[24]Vinokur, M., "Flux Jacobian Matrices and Generalized Roe Average for an Equilibrium Real Gas," NASA CR 117512, Dec. 1988.

[25]Grossman, B., and Walters, R. W., "Flux-Split Algorithms for the Multi-Dimensional Euler Equations with Real Gases," *Computers and Fluids*, Vol. 17, No. 1, 1989, pp. 99–112.

[26]Liou, M.-S., Van Leer, B., and Shuen, J.-S., "Splitting of Inviscid Fluxes for Real Gases," NASA TM 100856, April 1988.

[27]Carpenter, M., "A Generalized Chemistry Version of SPARK," NASA CR 4196, Dec. 1988.